

Report: Numerical Modeling and Simulation

Ravikiran Hegde

August 2025

1 Introduction

At the heart of atmospheric models lies the numerical solution of the Navier–Stokes equations, which govern fluid motion under the influence of pressure, gravity, and other forces. A simplified dynamical core provides the computational framework to integrate these equations together with thermodynamic and tracer evolution. In this project, I implement a two-dimensional solver that combines finite-difference discretizations with an FFT-based Poisson solver for pressure and third order Runge-Kutta time marching scheme. This forms the basis for a minimal atmospheric model, on which idealized experiments are performed to study convection, and circulation.

2 Theory

2.1 Anelastic Navier-Stokes Equations

The linearized equation of state for an ideal gas can be written as

$$\frac{\rho'}{\rho_0} = \frac{P'}{P_0} - \frac{T'_V}{T_{V0}}, \quad (1)$$

where $T_V = T \left[1 + \left(\frac{R_V}{R_D} - 1 \right) q_V - q_L \right]$ is the virtual temperature, and X' denotes the perturbation of a state variable X relative to the hydrostatic reference state X_0 . The reference state satisfies the ideal gas law, $P_0 = \rho_0 R_V T_{V0}$, and is in hydrostatic balance:

$$\frac{dP_0}{dz} = -\rho_0 g. \quad (2)$$

With the above anelastic approximation, the Navier-Stokes equation can be simplified as follows.

1. Continuity (Mass Conservation):

$$\nabla \cdot (\rho_0 \vec{v}) = 0 \quad (3)$$

2. Momentum Equation:

$$\rho_0 \left(\frac{\partial \vec{v}}{\partial t} + (\vec{v} \cdot \nabla) \vec{v} \right) = -\nabla P' + \rho' \vec{g} + \mu \nabla^2 \vec{v} \quad (4)$$

3. Internal Energy Equation:

$$\rho_0 \left(\frac{\partial U}{\partial t} + \vec{v} \cdot \nabla U \right) = -P' \nabla \cdot \vec{v} + \nabla \cdot (\vec{j}_h + \vec{j}_r) + Q_{\text{ext}} + \rho_0 L_v (\text{Cond} - \text{Evap}) \quad (5)$$

4. Moisture:

Vapour:

$$\rho_0 \left(\partial_t q_V + \vec{v} \cdot \nabla q_V \right) = \nabla \cdot (\rho_0 K_q \nabla q_V) - \rho_0 (\text{Cond} - \text{Evap}) \quad (6)$$

Liquid:

$$\rho_0 \left(\partial_t q_L + \vec{v} \cdot \nabla q_L \right) = \nabla \cdot (\rho_0 K_q \nabla q_L) - \rho_0 (\text{Prcp} - \text{Cond}) \quad (7)$$

2.2 Radiation

Prescribed cooling: I apply a uniform radiative tendency

$$\frac{\partial T}{\partial t} \Big|_{\text{rad}} = -2 \text{ K day}^{-1}, \quad (8)$$

used as a baseline cooling when radiative transfer is disabled.

Gray radiation: For prognostic runs, radiation is represented by a simplified gray monochromatic two-stream longwave scheme following Frierson et al. (2006). The model assumes a single longwave band with prescribed optical depth $\tau(p)$, no atmospheric shortwave absorption, and no radiative feedbacks from clouds or ozone. The longwave optical depth is pressure-scaled and includes both a linear component (well-mixed absorber, e.g. CO₂) and a quartic component (water-vapor-like, pressure-broadened), blended by f_ℓ :

$$\tau(P) = \tau_s \left[f_\ell \left(\frac{P}{P_{\text{surf}}} \right) + (1 - f_\ell) \left(\frac{P}{P_{\text{surf}}} \right)^4 \right], \quad 0 \leq f_\ell \leq 1. \quad (9)$$

The surface optical depth τ_s is specified with a latitudinal dependence to mimic meridional variations in greenhouse gas and water vapor distribution:

$$\tau_s(\phi) = \tau_{0E} + (\tau_{0P} - \tau_{0E}) \sin^2 \phi, \quad (10)$$

where τ_{0E} and τ_{0P} are the reference equatorial and polar optical depths, and ϕ is latitude.

The two-stream equations in optical-depth coordinates τ are

$$\frac{dF^\uparrow}{d\tau} = F^\uparrow - \sigma T^4, \quad \frac{dF^\downarrow}{d\tau} = -F^\downarrow + \sigma T^4, \quad (11)$$

with boundary conditions $F^\uparrow(\tau_s) = \sigma T_s^4$ at the surface and $F^\downarrow(0) = 0$ at the top of the atmosphere. The net longwave flux is $F_{\text{net}} = F^\uparrow - F^\downarrow$, and the corresponding radiative heating rate is

$$\frac{\partial T}{\partial t} \Big|_{\text{rad}} = -\frac{g}{c_p} \frac{\partial F_{\text{net}}}{\partial p} = \frac{1}{\rho c_p} \frac{\partial F_{\text{net}}}{\partial z}. \quad (12)$$

In addition to longwave cooling, a prescribed latitude-dependent shortwave forcing is included to represent the spatial distribution of incoming solar flux. The net solar flux (accounting for albedo) is

$$F_{\text{SW}}(\phi) = \frac{938}{4} \left[1 + \Delta_S P_2(\sin \phi) \right], \quad (13)$$

where $\Delta_S = 1.4$ sets the strength of meridional variation and $P_2(x) = \frac{1}{2}(3x^2 - 1)$ is the second Legendre polynomial. This formulation yields enhanced solar forcing in the tropics and reduced forcing at high latitudes, consistent with Earth's annual-mean insolation pattern. However, the atmosphere is approximated to be transparent to shortwave radiation.

2.3 Microphysics

The saturation vapor pressure over liquid water, $e_s(T)$, is computed using the Magnus–Teten formula:

$$e_s(T) = 610.94 \times \exp \left(17.625 \frac{T - 273.15}{T - 273.15 + 237.3} \right), \quad (14)$$

where T is the temperature in °K. From this, the saturation mixing ratio q_{vs} is obtained as

$$q_{vs}(T, P) = 0.622 \frac{e_s(T)}{P - e_s(T)}, \quad (15)$$

This represents the maximum mass of water vapor per unit mass of dry air that can exist at a given temperature and pressure.

To ensure that the model conserves mass and energy during condensation or evaporation, I define the excess vapor relative to saturation as

$$\delta q = \begin{cases} q_V^n - q_{vs}, & q_V^n > q_{vs}, \\ 0, & q_V^n \leq q_{vs}, \end{cases} \quad (16)$$

where q_V^n is the water vapor mixing ratio at the current time step. The adjustment then updates the vapor and liquid water content as

$$q_V^{n+1} = q_V^n - \delta q, \quad q_L^{n+1} = q_L^n + \delta q, \quad \Delta U = -L_v \delta q, \quad (17)$$

where L_v is the latent heat of vaporization. This saturation adjustment ensures that the water vapor does not exceed its saturation value, transferring any excess into liquid water while updating the internal energy to account for latent heat release.

3 Numerics

3.1 Finite difference operators

For a uniform grid with spacing Δx , the standard second-order centered finite difference approximations are given by:

$$\frac{\partial f}{\partial x}\Big|_i \approx \frac{f_{i+1} - f_{i-1}}{2\Delta x} \quad (18)$$

$$\frac{\partial^2 f}{\partial x^2}\Big|_i \approx \frac{f_{i+1} - 2f_i + f_{i-1}}{(\Delta x)^2} \quad (19)$$

Here, f_i is the function value at grid point i , $f_{i\pm 1}$ are the neighboring points, and the error in both cases is $\mathcal{O}(\Delta x^2)$.

Divergence operator is thus given by

$$\nabla \sim \frac{\partial}{\partial x} + \frac{\partial}{\partial z}. \quad (20)$$

and the Laplacian operator is given by

$$\nabla^2 \sim \frac{\partial^2}{\partial x^2} + \frac{\partial^2}{\partial z^2}. \quad (21)$$

3.2 Grid

I use a uniform 2-D spatial grid where x corresponds to the horizontal direction and z corresponds to the vertical dimension. All quantities are characterized at the cell center. The corresponding timestep, ΔT is calculated by considering the stability of the system as governed by Courant-Friedrichs-Lowy (CFL) stability constraint for advection and stability constraint for viscous diffusion. They are given by:

$$c \frac{\Delta t}{\min(\Delta x, \Delta dz)} < 1.73, \quad 4\nu \frac{\Delta t}{\min(\Delta x, \Delta dz)} < 2.57. \quad (22)$$

where c is the maximum velocity in the system, usually approximated as the speed of sound which is ≈ 340 m/s.

3.3 Boundary conditions

The system is periodic in x direction and non periodic in the z direction. The boundary conditions for different variables along the vertical dimension are listed in Table 1. To solve the pressure Poisson equation, and maintain divergence-free mass flux, i.e., $\nabla(\rho_0 \vec{v}) = 0$, the boundary conditions are derived from substituting the boundary conditions for \vec{v} at the top and bottom of the domain.

3.4 Poisson Solver

In the periodic x -direction, I apply a Fast Fourier Transform (FFT). This diagonalizes the derivative operator, reducing the problem to a set of independent equations for each wavenumber. Using the FFT allows us to efficiently compute derivatives and solve the Poisson equation in spectral space, exploiting the periodicity to avoid the need for iterative solvers in x .

In the non-periodic z -direction, the resulting equations from the spectral decomposition form tri-diagonal matrices for each Fourier mode, considering the Neumann boundary conditions to maintain a divergence-free mass flux. These are efficiently solved using a Thomas algorithm, which scales linearly with the number of grid points in z .

The resultant pressure field is then inverse Fourier transformed to obtain the solution in x - z space. This combination of spectral methods in periodic directions and direct tri-diagonal solvers in bounded directions provides a fast and accurate solution for the pressure field, ensuring that the updated velocity field satisfies the divergence-free condition.

Variable	Axis	Type	Value
u	bottom	Dirichlet	0.0 (no-slip)
	top	Dirichlet	0.0 (no-slip)
w	bottom	Dirichlet	0.0 (impermeable)
	top	Dirichlet	0.0 (impermeable)
U	bottom	Neumann	0.0 (adiabatic)
	top	Dirichlet	prescribed flux $c_v \vec{j}_r \cdot \hat{\mathbf{z}} / k_T$
q_V	bottom	Neumann	0.0
	top	Neumann	0.0
q_L	bottom	Neumann	0.0
	top	Neumann	0.0

Table 1: Boundary conditions.

3.5 Time marching

Taking the divergence of the momentum equation (4) together with the continuity equation (3) leads to the pressure Poisson equation in elliptic form:

$$\nabla \cdot (\rho_0 \nabla P') = \frac{1}{\Delta t} \nabla \cdot (\rho_0 \vec{v}^*), \quad (23)$$

where \vec{v}^* is the provisional (intermediate) velocity defined as

$$\vec{v}^* = \vec{v} + f(\vec{v}) \Delta t, \quad (24)$$

and $f(\vec{v})$ represents the non-pressure terms on the right-hand side of the momentum equation, including advection, buoyancy, and viscous effects:

$$f(\vec{v}) = \frac{\rho'}{\rho_0} \vec{g} - (\vec{v} \cdot \nabla) \vec{v} + \nu \nabla^2 \vec{v}. \quad (25)$$

This formulation separates the pressure contribution from the other forces, allowing the velocity update to be performed using the a projection method.

To enforce the divergence constraint (e.g., incompressibility), I use a projection step after each explicit Euler substep. The projection consists of solving a Poisson equation for the pressure correction P' and updating the velocity:

$$\vec{v}^{n+1} = \vec{v}^* - \frac{\Delta t}{\rho_0} \nabla P', \quad (26)$$

where \vec{v}^* is the intermediate velocity from the explicit step.

- Stage 1: First Euler step + projection

$$\vec{v}_1^* = \vec{v}^n + \Delta t f(\vec{v}^n), \quad (27)$$

$$\text{solve Poisson: } \nabla^2 P'_1 = \frac{\rho_0}{\Delta t} \nabla \cdot \vec{v}_1^*, \quad (28)$$

$$\vec{v}_1 = \vec{v}_1^* - \frac{\Delta t}{\rho_0} \nabla P'_1. \quad (29)$$

- Stage 2: Second RK3 stage + projection

$$\vec{v}_2^* = \vec{v}_1 + \Delta t f(\vec{v}_1), \quad (30)$$

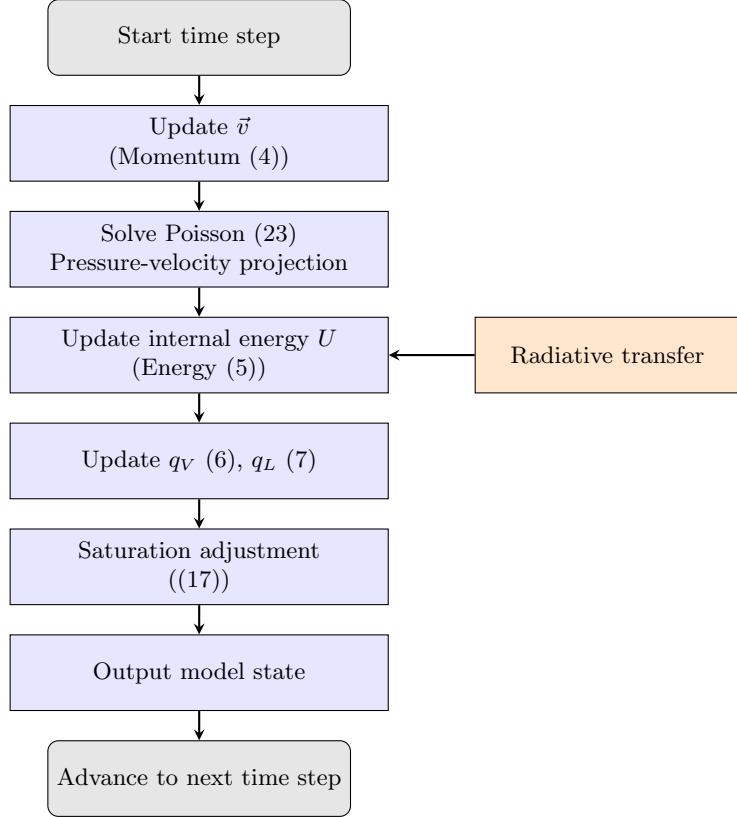


Figure 1: Order of processes at each time step

$$\text{solve Poisson: } \nabla^2 P'_2 = \frac{\rho_0}{\Delta t} \nabla \cdot \vec{v}_2^*, \quad (31)$$

$$\vec{v}_2^{\text{proj}} = \vec{v}_2^* - \frac{\Delta t}{\rho_0} \nabla P'_2, \quad (32)$$

$$\vec{v}_2 = \frac{3}{4} \vec{v}^n + \frac{1}{4} \vec{v}_2^{\text{proj}}. \quad (33)$$

- Stage 3: Final RK3 stage + projection

$$\vec{v}_3^* = \vec{v}_2 + \Delta t f(\vec{v}_2), \quad (34)$$

$$\text{solve Poisson: } \nabla^2 P'_3 = \frac{\rho_0}{\Delta t} \nabla \cdot \vec{v}_3^*, \quad (35)$$

$$\vec{v}_3^{\text{proj}} = \vec{v}_3^* - \frac{\Delta t}{\rho_0} \nabla P'_3 \quad (36)$$

$$\vec{v}^{n+1} = \frac{1}{3} \vec{v}^n + \frac{2}{3} \vec{v}_3^{\text{proj}}. \quad (37)$$

The final velocity \vec{v}^{n+1} is divergence-conforming and third-order accurate in time. \vec{v}^{n+1} and P' are then used to update the internal energy, moisture fields using the classical Runge-Kutta 3rd order time marching scheme following:

$$\begin{aligned} k_1 &= f(t_n, f^n) \\ k_2 &= f\left(t_n + \frac{\Delta t}{2}, f^n + \frac{\Delta t}{2} k_1\right) \\ k_3 &= f\left(t_n + \Delta t, f^n - \Delta t k_1 + 2\Delta t k_2\right) \\ f^{n+1} &= f^n + \frac{\Delta t}{6} (k_1 + 4k_2 + k_3) \end{aligned}$$

The time stepping algorithm is summarized in Figure 1

4 Experiments

Atmospheric Setup

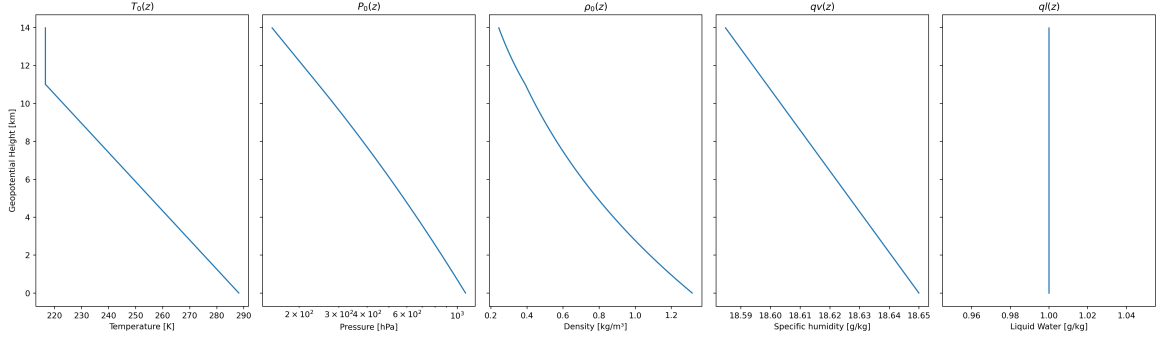


Figure 2: Initial vertical temperature profiles of the atmosphere at $\phi = 0$.

The model atmosphere is initialized using standard vertical profiles for temperature, water vapor, and liquid water content.

- Hydrostatic balance: The temperature follows the International Standard Atmosphere (ISA), defined from the surface up to approximately 85 km. Between specified levels, temperature values are interpolated. For heights or pressures outside this range, the profile is extrapolated linearly. This provides a realistic stratification of the atmosphere, including the troposphere and stratosphere.

The hydrostatic pressure profile is computed from the temperature profile as

$$P_0(z) = P_{\text{surf}} \exp \left[- \int_0^z \frac{g}{R_d T_0(z')} dz' \right]. \quad (38)$$

The corresponding air density is then obtained from the ideal gas law:

$$\rho_0(z) = \frac{P_0(z)}{R_d T_0(z)}. \quad (39)$$

These expressions ensure that the atmosphere is initially in hydrostatic balance with a realistic vertical temperature profile.

- Humidity Profile: The water vapor mixing ratio decreases with height according to an exponential–Gaussian profile following the Radiative–Convective Equilibrium Model Intercomparison Project (RCEMIP, Wing et al., 2017) :

$$q_v(z) = \begin{cases} q_0 \exp \left(-\frac{z}{z_{q1}} \right) \exp \left[-\left(\frac{z}{z_{q2}} \right)^2 \right], & z \leq z_t, \\ q_t, & z > z_t, \end{cases} \quad (40)$$

where q_0 is the surface mixing ratio, q_t the stratospheric value, z_t the tropopause height, and z_{q1}, z_{q2} shape parameters controlling the vertical decay. Near the surface, the mixing ratio is highest and decreases rapidly in the lower troposphere, becoming very small in the stratosphere. This captures the vertical variation of moisture in the atmosphere.

- Liquid Water Profile: The initial liquid water content is small background value. This allows the model to represent pre-existing cloud water in the atmosphere while keeping the rest of the domain essentially dry.

Together, these profiles provide physically consistent initial conditions for the model’s thermodynamic and moisture fields, ensuring realistic atmospheric stratification for subsequent experiments.

4.1 Warm Bubble

The warm bubble experiment initializes a localized temperature perturbation in an otherwise hydrostatic atmosphere. The perturbation is defined by a smooth, cosine-shaped bubble:

$$T'(\vec{x}) = \begin{cases} \frac{\Delta T}{2} \left[1 + \cos \left(\pi \frac{|\vec{x} - \vec{x}_c|}{R} \right) \right], & |\vec{x} - \vec{x}_c| < R, \\ 0, & |\vec{x} - \vec{x}_c| \geq R, \end{cases} \quad (41)$$

where $\vec{x}_c = (L_x/2, 3\text{ km})$ is the bubble center, $R = 1\text{ km}$ is the radius, and $\Delta T = 4\text{ K}$ is the temperature perturbation. The total initial temperature field is

$$T = T_0 + T'. \quad (42)$$

The perturbation in hydrostatic pressure is computed as

$$P' = P_{\text{surf}} \left[\exp \left(- \int_0^z \frac{g}{R_d T} dz \right) - \exp \left(- \int_0^z \frac{g}{R_d T_0} dz \right) \right], \quad (43)$$

and the internal energy is updated as

$$U = C_v T. \quad (44)$$

This setup produces a buoyant thermal that evolves under gravity, allowing study of convective initiation. The evolution of such a system is shown in Figure 3. The warm bubble moves up eventually taking a mushroom like shape. Due to some numerical inconsistency, the temperature field becomes highly stratified at the edge of the bubble around 3km leading to negative temperatures at some grid cells. The exact cause of this artifact is yet to be investigated.

4.2 Surface Temperature Gradient

The surface temperature gradient experiment imposes a meridional temperature variation to create a baroclinic forcing:

$$T'(\phi) = -\Delta T_{EP} \sin^2 \phi, \quad (45)$$

where ϕ is latitude, and $\Delta T_{EP} = 60\text{ K}$ represents the equator-to-pole surface temperature difference. The total temperature field is

$$T = T_0 + T'(\phi), \quad (46)$$

with the hydrostatic pressure perturbation again computed as

$$P' = P_{\text{surf}} \left[\exp \left(- \int_0^z \frac{g}{R_d T} dz \right) - \exp \left(- \int_0^z \frac{g}{R_d T_0} dz \right) \right], \quad (47)$$

and internal energy

$$U = C_v T. \quad (48)$$

From these fields, the base density and virtual temperature are

$$\rho_0 = \frac{P_0}{R_d T}, \quad T_v = T \left[1 + \left(\frac{R_v}{R_d} - 1 \right) q_v - q_l \right]. \quad (49)$$

This configuration generates a meridional gradient driving circulation in the domain.

The evolution of the system with and without coupled radiation scheme is shown in Figure 4.

The velocity mimics an overturning circulation from the warm regions where the air moves up and descents in the colder regions. A slight difference in the velocity structure can be noted at around 6 kms which is due to the nature of the horizontal variation of the vertical temperature profile. The numerical artifacts in temperature field also appear in these simulations, making it difficult to run long term simulations. The odd and even vertical levels show a decoupling leading to string differences in the temperature profile as shown in Figure 5 (b) and (c).

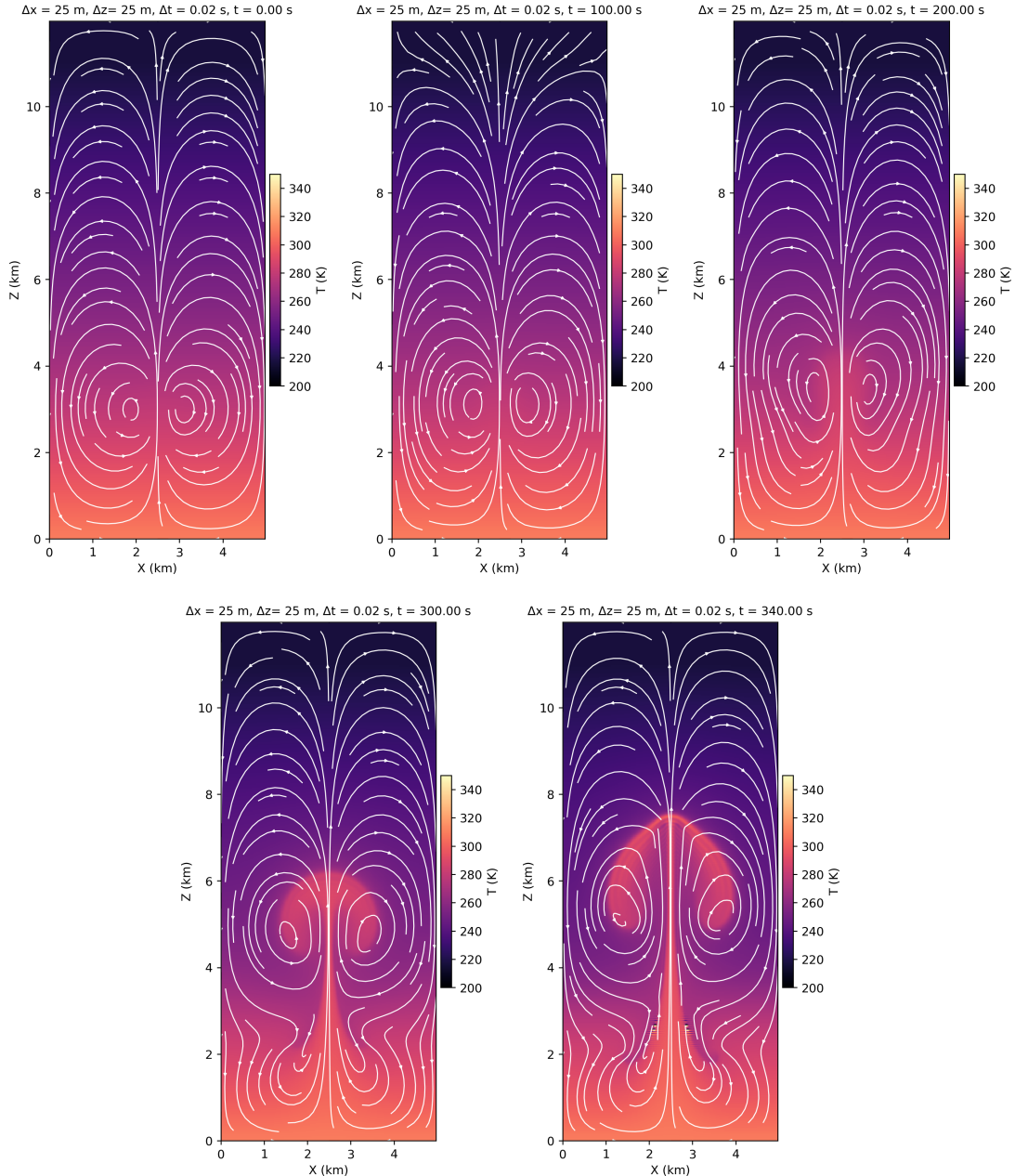


Figure 3: Warm bubble experiment: temporal evolution of the temperature field (shading) with velocity streamlines.

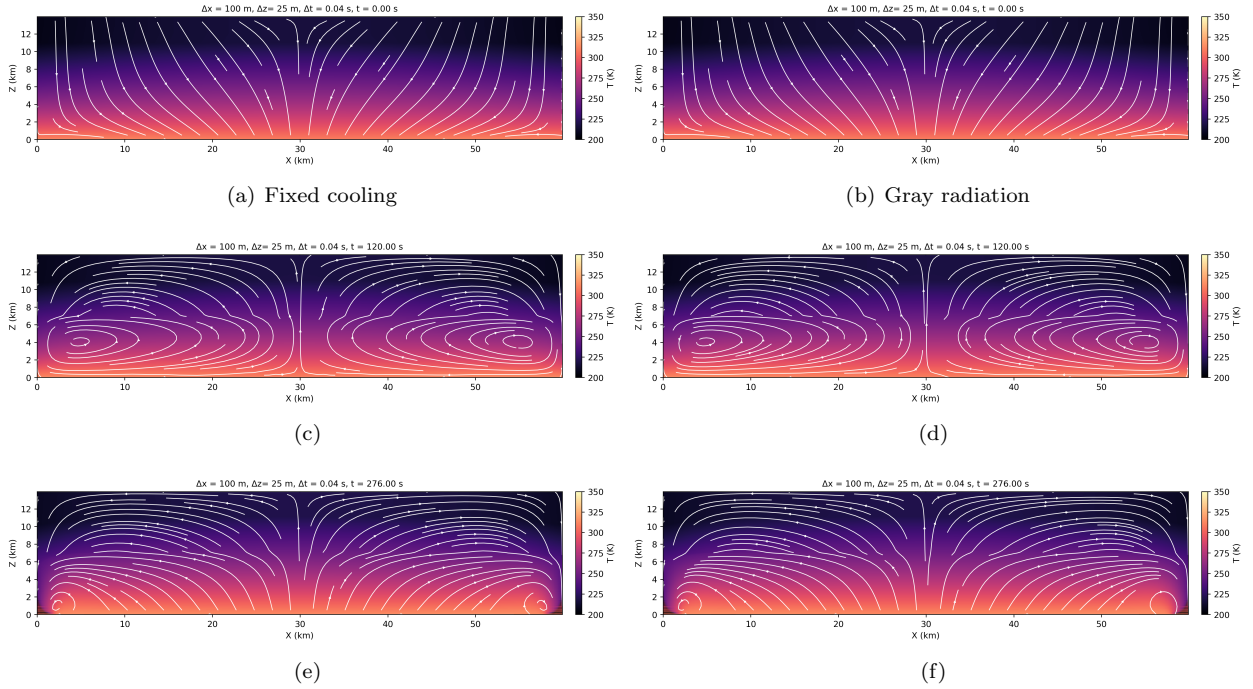


Figure 4: Comparison of temperature field and streamlines between fixed 2K/day cooling and gray radiation.

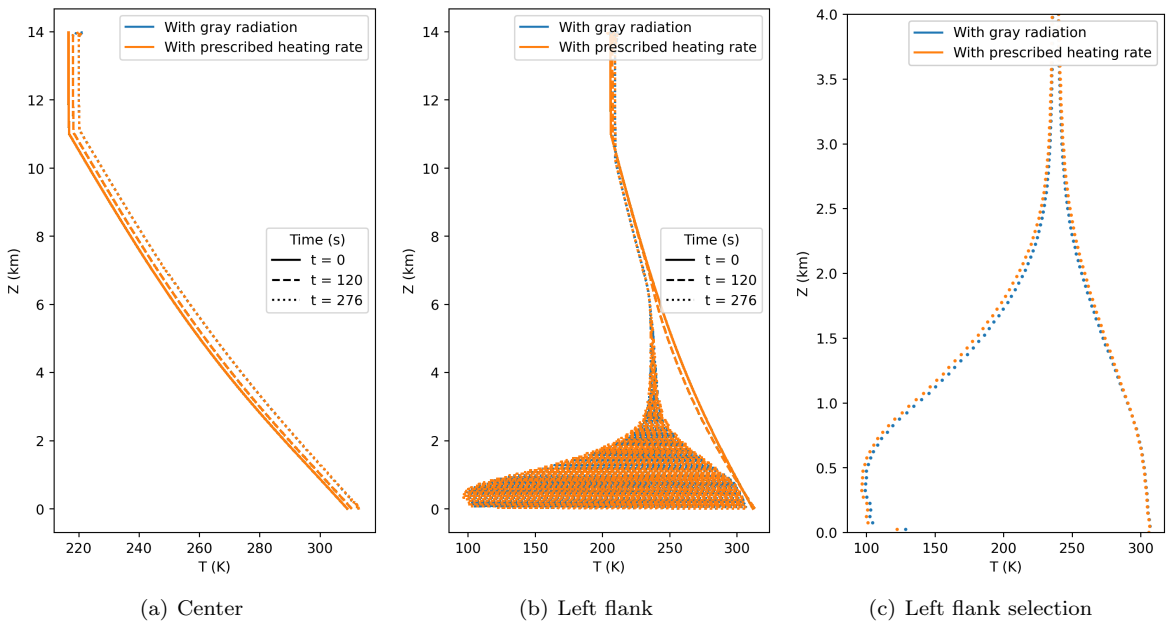


Figure 5: Vertical temperature profile comparisons between fixed cooling and gray radiation.

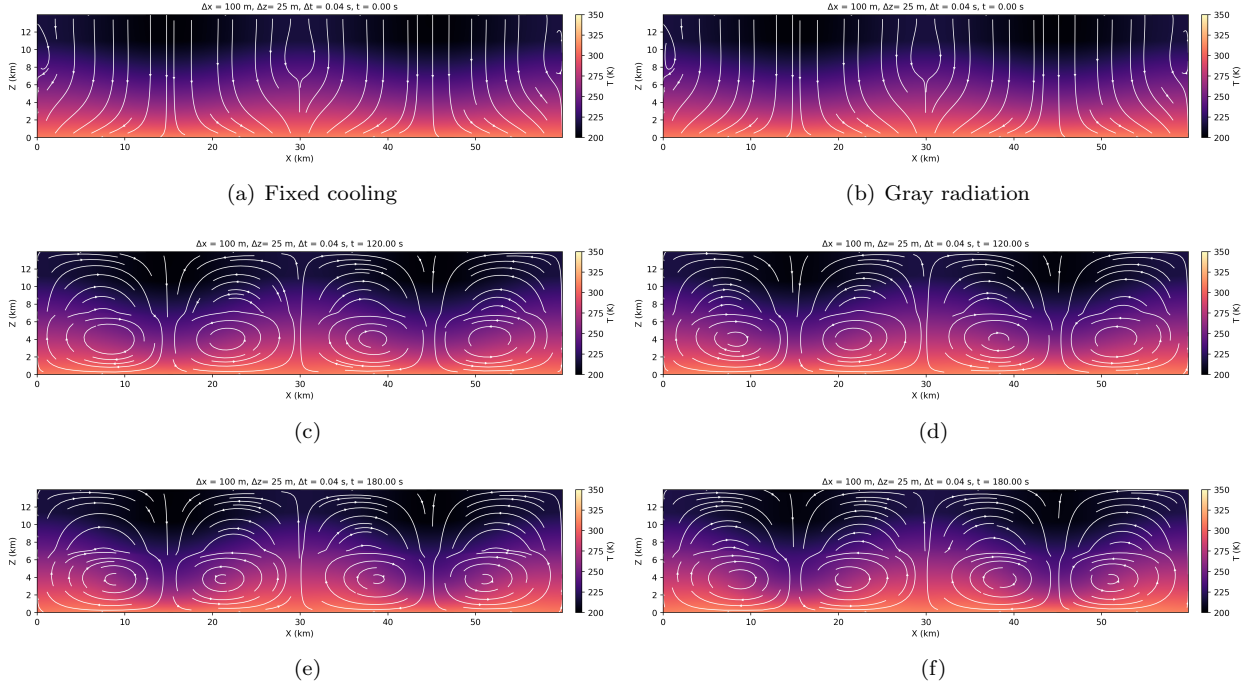


Figure 6: Comparison of the evolution of temperature field (two maxima and minima mimicking equator–pole structure) and velocity streamlines between fixed 2K/day cooling and gray radiation.

5 Conclusion

I have developed and tested the dynamical core of an idealized atmospheric model framework to study the interaction of dynamics and radiation under controlled settings. Three main experimental setups were considered: (i) the warm bubble test, demonstrating the model’s ability to capture buoyancy-driven convection and wave propagation; (ii) prescribed large-scale forcing experiments, where a fixed radiative cooling rate was contrasted with a prognostic gray–radiation scheme; and (iii) extended experiments with imposed meridional temperature gradients, mimicking equator–pole contrasts.

The warm bubble case validated the core dynamical solver and the efficiency of the Poisson pressure solution. The fixed-cooling and gray-radiation setups highlighted the role of radiative parameterizations in controlling the vertical temperature structure.

Several limitations were noted. The temperature field has certain local numerical artifacts leading to negative temperature and thus restricting long time scale simulations. It was also noted that the system is not stable when the domain length and resolutions were increased to planetary scales ($\sim 500 - 1000$ km). Due to the time restrictions, the exact causes have not been identified.

Overall, the model reproduces key features of convective adjustment, radiative balance, and large-scale circulation within a simplified yet flexible framework. These experiments establish a foundation for future extensions, including more realistic radiation schemes, large domain circulations, and interactive surface boundary conditions and a realistic treatment of the water cycle.

Code Availability

The full model source code, including scripts to reproduce the experiments and figures, is available at: <https://github.com/ravikiran-hegde/nums.git>.

Table 2: Symbols, units and values

Symbol	Description	Typical value / Units
\vec{v}	Velocity vector	m s^{-1}
ρ	Total density ($\rho = \rho_0 + \rho'$)	kg m^{-3}
ρ_0	Background hydrostatic density	kg m^{-3}
ρ'	Density perturbation	kg m^{-3}
P	Total pressure ($P = P_0 + P'$)	Pa
P_0	Hydrostatic (background) pressure profile	$\text{Pa}; P_{\text{surf}} = 108900 \text{ Pa}$
P'	Pressure perturbation	Pa
U	Specific internal energy ($U = c_v T$)	J kg^{-1}
T	Temperature	K
c_v	Specific heat at constant volume	$\approx 717 \text{ J kg}^{-1} \text{ K}^{-1}$
c_p	Specific heat at constant pressure	$\approx 1004 \text{ J kg}^{-1} \text{ K}^{-1}$
R_d	Gas constant (dry air)	$287 \text{ J kg}^{-1} \text{ K}^{-1}$
R_v	Gas constant (water vapour)	$461 \text{ J kg}^{-1} \text{ K}^{-1}$
L_v	Latent heat of vaporization	$\approx 2.5 \times 10^6 \text{ J kg}^{-1}$
g	Gravitational acceleration	9.81 m s^{-2}
μ	Dynamic viscosity ($\mu = \rho \nu$)	$\text{kg m}^{-1} \text{ s}^{-1}$
ν	Kinematic viscosity	$0.1 \text{ m}^2 \text{ s}^{-1}$
\vec{j}_h	Conductive heat flux ($\vec{j}_h = -k \nabla T$)	W m^{-2}
\vec{j}_r	Radiative heat flux	W m^{-2}
q_v	Water vapour mixing ratio (specific humidity)	kg kg^{-1}
q_l	Liquid water mixing ratio	kg kg^{-1}
q_{vs}	Saturation mixing ratio	kg kg^{-1}
δq	Condensed excess (saturation adjustment)	kg kg^{-1}
τ	Optical depth	dimensionless
τ_s	Surface optical depth	dimensionless
f_ℓ	Fraction of well-mixed longwave absorber	dimensionless, $0 \leq f_\ell \leq 1$
σ	Stefan–Boltzmann constant	$5.670374419 \times 10^{-8} \text{ W m}^{-2} \text{ K}^{-4}$
F_{net}	Net longwave flux ($F^\uparrow - F^\downarrow$)	W m^{-2}
F_{SW}	Net shortwave (surface) flux	W m^{-2} ; global mean = $\frac{938}{4} \approx 234.5$
Δ_S	Amplitude of latitudinal shortwave variation	1.4 (dimensionless)
Δt	Time step	s
$\Delta x, \Delta z$	Grid spacings (horizontal, vertical)	m